Photometric study of the late-time near-infrared plateau in Type Ia supernovae

M. Deckers [1]★ O. Graur [2,3] K. Maguire [1] L. Shingles [4] S. J. Brennan [5,6] J. P. Anderson,[7,8]
J. Burke,[9,10] T.-W. Chen,[11,12] L. Galbany,[13,14] M. J. P. Grayling [15,16] C. P. Gutiérrez,[17,18] L. Harvey [1]
D. Hiramatsu,[19,20] D. A. Howell,[9,10] C. Inserra [21] T. Killestein [22] C. McCully,[10]
T. E. Müller-Bravo,[13,14] M. Nicholl [23] M. Newsome,[9,10] E. Padilla Gonzalez,[9,10] C. Pellegrino,[9,10]
G. Terreran [9,10] J. H. Terwel [1,24] M. Toy [15] and D. R. Young[25]

Affiliations are listed at the end of the paper

ABSTRACT

We present an in-depth study of the late-time near-infrared plateau in Type Ia supernovae (SNe Ia), which occurs between 70 and 500 d. We double the existing sample of SNe Ia observed during the late-time near-infrared plateau with new observations taken with the Hubble Space Telescope, Gemini, New Technology Telescope, the 3.5-m Calar Alto Telescope, and the Nordic Optical Telescope. Our sample consists of 24 nearby SNe Ia at redshift < 0.025. We are able to confirm that no plateau exists in the K_s band for most normal SNe Ia. SNe Ia with broader optical light curves at peak tend to have a higher average brightness on the plateau in J and H, most likely due to a shallower decline in the preceding 100 d. SNe Ia that are more luminous at peak also show a steeper decline during the plateau phase in H. We compare our data to state-of-the-art radiative transfer models of nebular SNe Ia in the near-infrared. We find good agreement with the sub-M_{ch} model that has reduced non-thermal ionization rates, but no physical justification for reducing these rates has yet been proposed. An analysis of the spectral evolution during the plateau demonstrates that the ratio of [Fe II] to [Fe III] contribution in a near-infrared filter determines the light curve evolution in said filter. We find that overluminous SNe decline slower during the plateau than expected from the trend seen for normal SNe Ia.

Key words: Surveys – supernovae: general.

1 INTRODUCTION

Although Type Ia supernovae (SNe Ia) are widely used as cosmic distance indicators (Riess et al. 1998; Perlmutter, Turner & White 1999), there is still debate about their explosion mechanisms and the nature of their progenitors (see Hillebrandt et al. 2013; Maoz, Mannucci & Nelemans 2014; Jha, Maguire & Sullivan 2019; Ruiter 2020 for comprehensive reviews). It is generally accepted that SNe Ia originate from the thermonuclear explosions of carbon–oxygen white dwarfs (CO WDs). The CO material burns to iron-group elements, and the radioactive decay of $^{56}Ni \rightarrow ^{56}Co$ ($t_{1/2} = 6$ d) powers the early light curves of SNe Ia. Around 60 d post explosion, the dominating radioactive decay chain shifts to the decay from $^{56}Co \rightarrow ^{56}Fe$, with a longer half-life of 78 d.

In the nebular phase (phase > 150 d), the outer layers of the SN ejecta become transparent and the inner regions of the ejecta become visible. Late-time spectroscopy can be used to search for hydrogen, which would point towards a single-degenerate scenario (Hamuy et al. 2003; Mattila et al. 2005; Leonard 2007; Lundqvist et al. 2013; Shappee et al. 2013; Silverman et al. 2013; Lundqvist et al. 2015; Maguire et al. 2016; Graham et al. 2019; Kollmeier

et al. 2019; Prieto et al. 2020). Late-time spectra can also be used to constrain the amount of stable nickel versus unstable material, which can be compared to predictions from explosion models where a larger ratio points to burning at higher central densities, implying a larger progenitor mass (Mazzali et al. 2015; Botyánszki & Kasen 2017; Maguire et al. 2018; Flörs et al. 2020).

The majority of studies at all epochs focus on the optical, because SNe Ia are brightest at these wavelengths and there are many optical instruments available. Studying the near-infrared (NIR, $\lambda > 0.8$ μm) is more difficult, but is beneficial because SNe Ia are better standard candles in this wavelength range (Elias et al. 1981, 1985; Krisciunas, Phillips & Suntzeff 2004; Wood-Vasey et al. 2008; Barone-Nugent et al. 2012; Johansson et al. 2021; Galbany et al. 2022; Jones et al. 2022; Müller-Bravo et al. 2022). They are less impacted by extinction, with inferred distance estimate root mean square values dropping by 2–4σ even before any corrections are applied to the light curves (Avelino et al. 2019).

While most NIR studies focus on light-curve standardization around peak (−5–40 d), observations around 70–600 d are very important for understanding the evolution of the ejecta. Our understanding of the NIR evolution of SNe Ia at late times has evolved significantly during the past four decades. Axelrod (1980) predicted an 'IR-catastrophe' – a shift from optical and NIR emission lines to fine-structure iron lines in the mid and far-IR that occurs at

★ E-mail: deckersm@tcd.ie

around 450 d due to an onset of thermal instability that causes a dramatic temperature change from ∼3000 K to ∼300 K. However, the resulting sharp decline in the optical and NIR light curves has never been observed in SNe Ia. Graur et al. (2020) found instead that SNe Ia reach a plateau in the *J* and *H* bands starting at ∼150 d and lasting for approximately a year. The presence of a plateau in the NIR was first predicted by Fransson, Houck & Kozma (1996), where it was linked to the onset of the IR-catastrophe.

Fransson et al. (1996) suggested the flattening of the *J* band is due to the shift from emission of [Fe III] at ∼5000 Å to emission of [Fe II] at 1.257 μm and 1.644 μm, which is supported by the NIR evolution of SN 2014J presented by Diamond et al. (2018). Updated spectral models by Fransson & Jerkstrand (2015) showed that a redistribution of ultra-violet (UV) emissivity increases the flux in the optical and NIR, circumventing the 'IR-catastrophe'.

This flux-redistribution behaviour is reminiscent of the re-brightening seen in the NIR around 30 d past maximum, also called the secondary maximum. This feature is caused by sharp peaks in the emissivity of iron/cobalt gas at certain temperatures, which are near an ionization edge (Kasen 2006). The dependence of the emissivity on temperature explains why for subluminous and cooler 1991bg-like SNe Ia (Filippenko et al. 1992; Leibundgut et al. 1993; Turatto et al. 1996; Taubenberger 2017), the secondary maximum is shifted to earlier phases, often causing it to blend with the primary maximum. The strongest peak in the NIR emissivity occurs at ∼7000 K and represents the ionization edge between doubly ionized to singly ionized iron, when the ejecta becomes very efficient at redistributing flux from the UV to longer wavelengths, which leads to the re-brightening in the NIR during the secondary maximum. Another peak exists at the ionization edge between singly ionized and neutral iron at ∼2500 K, which may coincide with the onset of the NIR plateau at ∼150 d. Diamond et al. (2018) presented NIR spectra of SN 2014J during the plateau phase, which demonstrated a decrease in the strength of [Fe III] features in favour of [Fe II] features, but no [Fe I] features. Sollerman et al. (2004) and Graur et al. (2020) agreed that the scattering of UV photons to longer wavelengths is the most likely cause of the NIR plateau.

The end of the plateau at ∼500 d is not yet understood, although a tentative detection of [Fe I] by Graur et al. (2020) suggested a third shift in the dominant ionization state of iron. Tucker et al. (2022) also identified strengthening features in the optical after the end of the plateau that could be attributed to [Fe I].

Graur et al. (2020) tentatively suggested that the plateau does not extend to the K_s-band, and that the plateau in the *H* band is comprised of two distinct branches. No theoretical explanation for this bimodal behaviour was offered, although a correlation between the peak magnitude and the magnitude of the plateau would align well with the idea that the plateau is caused by a similar mechanism as the secondary maximum.

In this paper, we extend the sample of SNe Ia with NIR photometry on the late-time plateau to 24 SNe Ia, and use the additional data to confirm the absence of the plateau in the K_s band, and test whether the magnitudes in the *H*-band plateau consist of two distinct branches as suggested by Graur et al. (2020). In Section 2, we introduce the sample of nearby SNe Ia and describe the late-time NIR photometry and spectroscopy included in this paper. Fitting methods implemented in this work, as well as the radiative transfer models of SNe Ia in the nebular phase that we compare to our data are described in Section 3. We present our results in Section 4 and discuss their implications in a theoretical context in Section 5. Finally, we summarize and conclude in Section 6.

2 DATA

In Section 2.1, we present the sample of nearby SNe Ia used in this paper. We describe the spectra and photometry included in this paper, which is a combination of data pulled from the literature and new data, in Section 2.2.

2.1 Sample of nearby SNe Ia

Our sample consists of new data, as well as data that have previously been published, totalling 24 SNe Ia. Of these, 20 are classified as normal SNe Ia, two are classified as 91T-like (SNe 2000cx and 2021wuf), and two are classified as transitional objects (SNe 2004eo and 2012ht). The NIR photometry of six SNe Ia (SNe 2020ees, 2020uxz, 2021jad, 2021pit, 2021wuf, and 2021aefx) and XShooter spectra of two SNe Ia (SNe 2016hvl and 2017cbv) are presented for the first time in this paper. XShooter spectra of three SNe (SNe 2012cg, 2012ht, and 2013aa) published by Maguire et al. (2013) and spectra of four SNe (SNe 2012fr, 2013cs, 2013ct, and 2013dy) published by Maguire et al. (2016) are also included. We performed synthetic photometry on these spectra to extract NIR photometry as described in Section 2.2.2. We include NIR photometry for 10 SNe Ia presented by Graur et al. (2020) (SNe 2000cx, 2001el, 2004eo, 2011fe, 2012ht, 2013dy, 2014J, 2017erp, 2018gv, and 2019np, which were originally published by Krisciunas et al. 2003; Sollerman et al. 2004; Pastorello et al. 2007; Stritzinger & Sollerman 2007; Sand et al. 2016; Shappee et al. 2017; Burns et al. 2018). We note that the NIRI observations of SN 2020uxz were taken in *K* rather than K_s. The early observations of SN 2001el (Krisciunas et al. 2003) are taken in a mixture of *K* and K_s, but here we only include the data taken in K_s. The late-time observations from Stritzinger & Sollerman (2007) are taken exclusively in K_s. We never mix *K* and K_s data when performing fits, as will be discussed further in Section 4. An overview of the sample is presented in Table A1.

Observing the NIR plateau is difficult because SNe Ia are inherently fainter in the NIR compared to the optical and by 150 d they have faded by ∼6 magnitudes relative to peak. Consequently, all the SNe Ia in our sample are nearby, have $m_{max}^B < 15$ mag (with the exception of SN 2016hvl, which has $m_{max}^B = 15.4$ mag), and are offset from their host galaxies to reduce host contamination. We note that the last criterion is one potential source of bias in our sample (Wang et al. 2013).

All distance moduli and uncertainties were taken either from the literature where available, or calculated from redshift-independent distances provided by the NASA/IPAC Extragalactic Database (NED).[1] The data sources for the distance moduli are summarized in Table A1.

2.2 Observations

We report NIR photometry obtained using Wide-Field Camera 3 (WFC3) on the *Hubble Space Telescope* (*HST*), SOFI on the New Technology Telescope (NTT),[2] FLAMINGOS-2 (F2, Eikenberry et al. 2008) at Gemini-South, NIRI at Gemini-North (Hodapp et al. 2003), and Omega2000 on the 3.5-m Calar Alto Telescope (CA, Bailer-Jones, Bizenberger & Storz 2000; Baumeister et al. 2003;

---

[1]https://ned.ipac.caltech.edu/
[2]Data taken from the NTT were taken under the framework of the advanced Public ESO Spectroscopic Survey for Transient Objects (ePESSTO + , Smartt et al. 2015).

Table 1. Overview of NIR photometry obtained with *HST*. A machine-readable version of this table is available in the online material.

SN	MJD [d]	Phase[a] [d]	Filter	Exposure time [s]	Magnitude [mag]
2020ees	58931.7	5.6	F125W	46	16.928(005)
2020ees	58931.7	5.6	F160W	86	17.056(005)
2020ees	58936.7	10.6	F125W	46	17.539(007)
2020ees	58936.7	10.6	F160W	86	17.486(006)
2020ees	59330.9	404.8	F125W	1006	23.066(037)
2020ees	59330.9	404.8	F160W	1006	22.822(042)
2020ees	59330.9	404.8	F350LP	334	24.681(036)
2020ees	59439.3	513.2	F125W	1006	24.46(11)
2020ees	59439.3	513.2	F160W	1006	23.420(075)
2020ees	59439.3	513.2	F350LP	334	26.57(12)
2020uxz	59150.2	7.2	F125W	18	14.747(002)
2020uxz	59150.2	7.2	F160W	29	14.720(003)
2020uxz	59374.5	231.5	F336W	324	20.713(022)
2020uxz	59374.5	231.5	F350LP	300	19.554(003)
2020uxz	59374.5	231.5	F125W	203	20.617(010)
2020uxz	59374.5	231.5	F160W	406	20.265(013)
2020uxz	59485.2	342.2	F336W	330	22.154(051)
2020uxz	59485.2	342.2	F350LP	330	21.065(006)
2020uxz	59485.2	342.2	F125W	306	20.698(011)
2020uxz	59485.2	342.2	F160W	306	20.200(015)
2021jad	59623.0	294.3	F160W	356	19.388(430)
2021jad	59819.0	490.3	F160W	356	19.737(430)
2021jad	59973.5	644.8	F160W	356	21.581(037)
2020pit	59630.0	245.5	F160W	431	18.594(050)
2020pit	59832.0	447.5	F160W	431	19.428(050)
2020pit	59987.4	602.9	F160W	431	21.941(037)

Note. [a] Phase is defined as the time since maximum light in the *B* band (MJD - t_0).

Kovács et al. 2004) at the Centro Astronómico Hispano de Andalucía (CAHA), the Nordic Optical Telescope (NOT, Djupvik & Andersen 2010), as well as spectra obtained with XShooter on the Very Large Telescope (VLT) at the Paranal Observatory (Vernet et al. 2011). The NIR photometry and spectroscopy are described in Sections 2.2.1 and 2.2.2, respectively.

2.2.1 NIR Photometry

Table 1 shows the photometry of SNe 2020ees, 2020uxz, 2021jad, and 2021pit observed with WFC3 in the *F125W* and *F160W* filters, which can be approximated by the *J* and *H* bands, respectively (program ID's: GO-16497 and 16885, PI: Graur). We obtained photometry of SNe 2021jad, 2021pit, and 2021aefx with SOFI, which is an NIR spectrograph and imaging camera on the NTT (proposal ID's 1103.D-0328, 106.216C, and 108.220C, PI: Inserra). SN 2021pit was observed with F2 at Gemini-South (proposal ID: GS-2021B-FT-212, PI: Graur). *H*-band photometry of SN 2020uxz and SN 2021wuf were obtained with NIRI at Gemini-North (proposal ID's: GN-2021A-FT-114 and GN-2022A-FT-210, PI: Graur and Deckers). Finally, SN 2020uxz was observed with Omega2000 (proposal ID: H20-3.5-002, PI: Galbany). SN 2020uxz was also observed with the NOT (proposal ID: 62–202, PI: Galbany). The photometry obtained with SOFI, F2, NIRI, Omega2000, and NOT are summarized in Table 2.

All the photometry measurements were obtained using the package AUTOPHOT (Brennan & Fraser 2022).[3] The data were

[3] https://github.com/Astro-Sean/autophot

calibrated using the 2MASS catalogue in the Vega magnitude system. Since none of the sources are in very crowded fields, we implemented aperture photometry for the whole sample. As an additional test, point-spread function (PSF) photometry was performed where possible and compared to the aperture photometry. The aperture and PSF magnitudes were consistent within the uncertainties for all measurements. All sources are bright and far removed from their host galaxy and therefore template image subtraction was not required. Background surface fitting failed for a subset of the sample due to the noisy nature of the NIR images, so we reverted to local background fitting for the whole sample.

No S-corrections were applied to the *HST* photometry because no synchronous *J/F125W* or *H/F160W* data were available. We estimate the systematic offset between the filters by performing synthetic photometry on all the XShooter spectra in our sample for the *J, H, F125W*, and *F160W* bands. On average, we find that the *F125W* photometry is 0.3 mag fainter than the *J* band, and *F160W* is 0.4 mag fainter than the *H* band. We do not correct for these offsets but any *HST* photometry is highlighted in Fig. 1 and the reader should note that these points are expected to be fainter than the corresponding ground-based filters.

Finally, all the data were corrected for Milky Way extinction using the dust map provided by Schlafly & Finkbeiner (2011) and the Python module DUSTMAPS (Green 2018). The photometry was not corrected for host galaxy extinction because all the SNe are well separated from their host, and NIR photometry is minimally impacted by extinction. All the new NIR light curves, together with the NIR light curve data presented by Graur et al. (2020), are shown in Fig. 1.

Table 2. Overview of NIR photometry obtained with Gemini, the New Technology Telescope (NTT), and Calar Alto observatory. A full, machine-readable version of this table is available in the online material.

SN	MJD [d]	Phase [d]	Filter	Exposure time [s]	Magnitude [mag]	Instrument
2020uxz	59178.0	35.0	J	60	15.29(45)	NOTCAM
2020uxz	59178.0	35.0	H	60	14.43(45)	NOTCAM
2020uxz	59184.9	41.9	J	600	15.50(09)	Omega2000
2020uxz	59184.9	41.9	H	900	14.84(05)	Omega2000
2020uxz	59434.6	291.6	H	111	19.60(35)	NIRI
2020uxz	59434.6	291.6	J	111	19.82(39)	NIRI
2020uxz	59434.6	291.6	K	298	19.55(22)	NIRI
2021aefx	59563.3	17.4	J	32	14.23(13)	SOFI
2021aefx	59563.3	17.4	H	32	13.02(18)	SOFI
2021aefx	59591.0	45.1	J	24	14.26(10)	SOFI
2021aefx	59591.0	45.1	H	24	13.48(19)	SOFI
2021aefx	59591.0	45.1	K_s	60	13.52(02)	SOFI
2021aefx	59612.1	66.2	J	32	15.67(12)	SOFI
2021aefx	59612.1	66.2	H	32	14.35(20)	SOFI
2021aefx	59640.1	94.2	J	32	17.03(13)	SOFI
2021aefx	59640.1	94.2	H	32	10.75(33)	SOFI
2021aefx	59640.1	94.2	K_s	60	11.30(08)	SOFI
2021aefx	59649.1	103.2	H	144	16.46(48)	SOFI
2021aefx	59661.0	115.1	J	60	>15.5*	SOFI
2021aefx	59661.0	115.1	H	144	16.42(20)	SOFI
2021aefx	59661.1	115.2	K_s	160	15.97(19)	SOFI
2021aefx	59816.3	270.4	J	1080	18.89(24)	SOFI
2021aefx	59816.3	270.4	H	1440	18.31(18)	SOFI
2021aefx	59816.3	270.4	K_s	1440	18.33(21)	SOFI
2021jad	59492.3	163.6	J	1080	18.81(16)	SOFI
2021jad	59492.3	163.6	H	1440	17.81(11)	SOFI
2021jad	59513.3	184.6	J	1080	19.16(15)	SOFI

Note. * We found a very large uncertainty on the magnitude (18.5 ± 3.0 mag) for one *J*-band image of SN 2021aefx at MJD = 59661.0 d. This is likely because the source was faint and the exposure time (60 s) was not sufficient. The next data point at MJD = 59816.3 d has a similar magnitude (18.89 ± 0.24 mag) but was exposed for 1080 s and has a significantly smaller uncertainty. We quote this data point as an upper limit at 15.5 mag.

2.2.2 *Spectroscopy*

We include 12 mid-resolution spectra of eight SNe Ia obtained using XShooter. Eight of these spectra were previously presented by Maguire et al. (2013, 2016). Four spectra are published here for the first time and were reduced using the same method described by Maguire et al. (2016). Due to the relatively high-spectral resolution of XShooter ($\sim$35 km s^{-1}), host galaxy features were easily identified and removed in the reduction process (Maguire et al. 2016). We do not expect to see any contribution from a potential companion star since the remnant models presented in Pan, Ricker & Taam (2012) predict that the contribution will be very faint relative to the SN at these phases. The spectral response of XShooter is relatively stable with a relative flux uncertainty across the spectrum of 5 per cent (Vernet et al. 2011). The three arms of the XShooter spectrograph were firstly combined using their overlap wavelength regions with small scalings in their flux levels. Next, the spectra were flux calibrated using photometry from Las Cumbres Observatory Global Telescope Network (LCO; Brown et al. 2013) if possible, or alternatively, using photometry performed on stars in the Sloan Digital Sky Survey (SDSS) or Pan-STARRS1 (PS1) field of the acquisition image. As a last resort, zero-points were taken from XShooter.

The XShooter acquisition image of each SN was used to estimate the magnitude of the SN and comparison stars in the field of the SN. The spectra of SNe 2012cg, 2012ht, and 2013ct were calibrated by comparison of the companion stars to catalogue magnitudes from the SDSS Data Release 10 (Ahn et al. 2014), and the spectrum of

SN 2016hvl was calibrated by comparison to the PS1 Data Release 2 catalogue (Flewelling et al. 2020). The spectrum of SN 2017erp was calibrated to LCO photometry of the SN itself taken at similar phases to the spectral observation. The spectra of SNe 2012fr, 2013aa, and 2013cs were calibrated using the XShooter zero-points because no coeval SN photometry nor catalogue magnitudes from SDSS or PS1 were available. In these cases, the tabulated XShooter zero-point was used, resulting in a larger uncertainty. The uncertainty was estimated by comparing the magnitudes obtained using the zero-point method for SNe that also had catalogue measurements. These were found to be <0.5 mag, which we set as the conservative uncertainty of the magnitudes estimated using the zero-point method. The different sources for flux calibration result in a large range of uncertainties. A summary of the flux calibrations is presented in Table 3.

XShooter spectra extend from 5000 Å to 25 000 Å, but in some cases the spectrum is very noisy at the far red end. We excluded spectra with spurious flux values at the red edge of the detector by visual inspection. We used SNCOSMO (Barbary et al. 2022) to integrate across the *J*, *H*, and K_s 2MASS bandpasses to obtain synthetic photometry (see Table 3 and Fig. 1).

3 METHODS

In Section 3.1, we describe how we fit the NIR data to determine if there is a plateau, and how we derive the average magnitude and
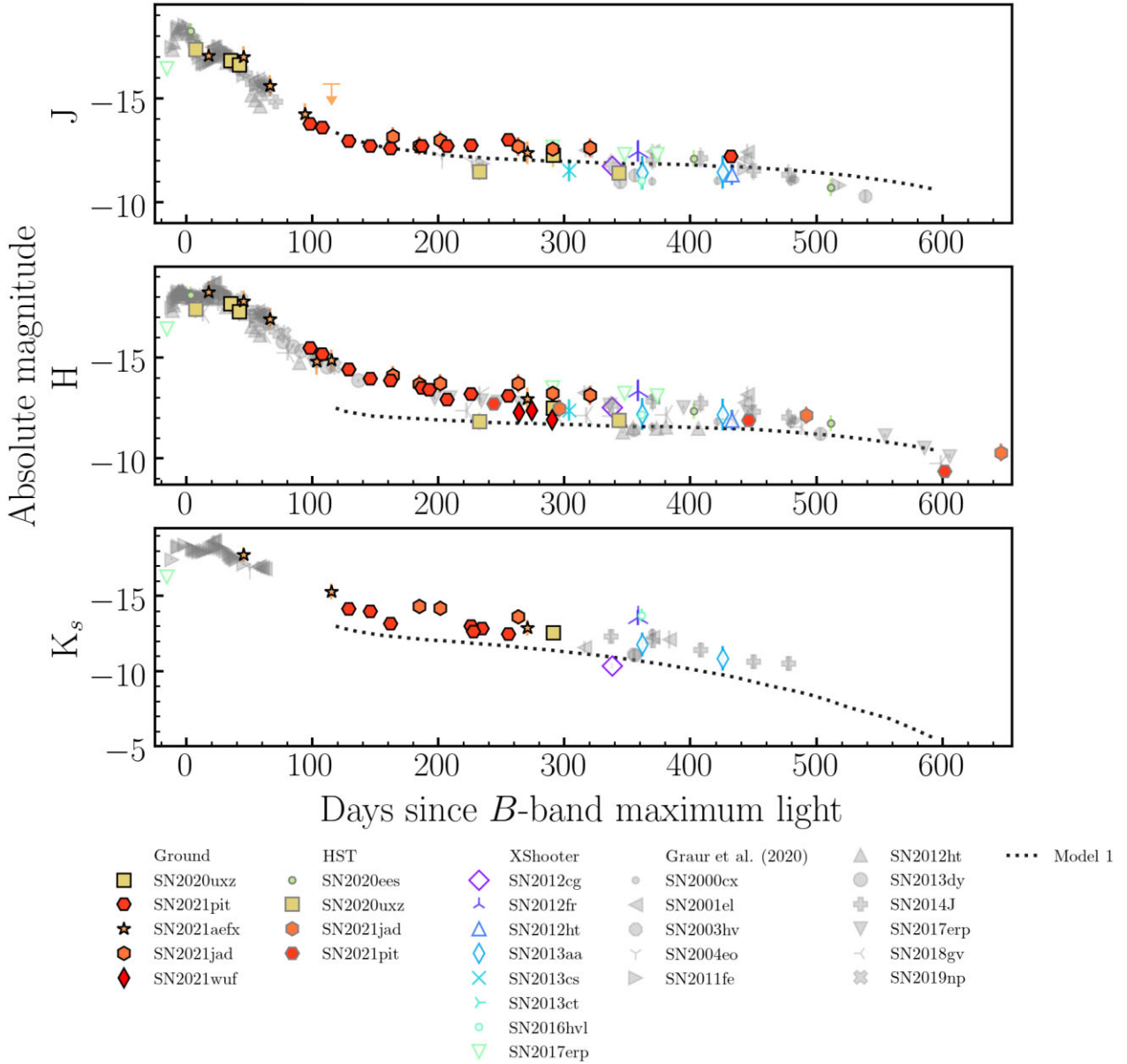
Figure 1. We present an overview of the J-, H-, and K_s-band light curves in absolute magnitude for all the SNe Ia in our sample. We note that the NIRI photometry of SN 2020uxz is taken in K rather than K_s. We also include a comparison to the sub-M$_{ch}$ model with 8× heatboost that best-matched SN 2013ct from Shingles et al. (2022). The model is scaled to our photometry in the J band.

Table 3. Overview of synthetic NIR photometry obtained with XShooter.

SN	MJD [d]	Phase [d]	J [mag]	H [mag]	K_s [mag]	Flux calibration uncertainty [mag]	Source of flux calibration
2012cg	56420.0	337.8	19.09	18.29	20.48	0.2	SDSS
2012fr	56600.0	358.1	18.93	18.03	17.81	0.5	XShooter zero-point
2012ht	56728.0	432.9	20.60	20.01	–	0.5	SDSS
2013aa	56704.0	361.5	19.30	18.53	18.94	0.8	XShooter zero-point
2013aa	56768.0	425.5	19.29	18.56	19.87	0.5	XShooter zero-point
2013cs	56741.0	303.8	21.41	20.55	–	0.5	XShooter zero-point
2013ct	56615.0	198.9	18.40	17.38	17.23	0.2	SDSS
2016hvl	58072.3	361.4	22.74	21.60	20.06	0.2	PS1
2017erp	58225.3	290.7	19.68	18.83	–	0.2	LCO Photometry
2017erp	58282.2	347.6	20.05	19.12	–	0.1	LCO Photometry
2017erp	58308.1	373.5	20.03	19.23	–	0.1	LCO Photometry

decline rate of the plateau. In Section 3.2, we describe SALT3 fits performed on the optical light curves around peak. We describe the radiative transfer models of SNe Ia in the nebular phase, which were first presented by Shingles et al. (2022) in Section 3.3.

3.1 Fitting the NIR data

To determine whether a light curve displays a plateau, and if so, when the transition onto the plateau occurs, we performed one- and two-component fits to the light curves between 30 and 500 d using a Markov Chain Monte Carlo (MCMC) using the package EMCEE (Foreman-Mackey et al. 2013). If a two-component fit is preferred over a one-component fit, we classify the light curve as having a plateau. We opted to use MCMC to perform these fits to obtain robust estimates of the uncertainties on each parameter.

For the one-component fit, we fit the following equation to $m^x(t)$, the magnitude in filter x at time t:

$$m^x(t) = s_2 t + b_2,$$ (1)

where s_2 is the slope and b_2 is the y-intercept. For the two-component fit, we implemented the same method as that used by Anderson et al. (2014) for characterizing the light curves of SNe II. The two-component fit is described by the following piece-wise function:

$$m^x(t) = \begin{cases} s_1 t + b_1 & \text{if } t <= t_0^x \\ s_2 t + b_2 & \text{if } t > t_0^x, \end{cases}$$ (2)

where s_2 and b_2 are the same as for the one-component fit, and s_1 and b_1 are the slope and y-intercept of the function prior to the transition onto the plateau. The time of the onset of the plateau in filter x, t_0^x is defined as follows:

$$t_0^x = \frac{b_2 - b_1}{s_1 - s_2}$$ (3)

to ensure that the two linear components intersect at t_0^x.

We ran an MCMC using 10 walkers for 10 000 iterations and uninformative priors. To avoid biasing the estimates of the slope during the plateau, we exclusively used data taken in J/H or $F125W/F160W$. We required at least four data points to perform the two-component fit since we are fitting for four parameters, and we required at least one data point at <150 d and one at >150 d to ensure we are sampling the phase ranges at either side of the expected transition onto the plateau. Only SNe 2001el, 2011fe, 2012ht, 2014J, 2018gv, 2021pit, and 2021aefx had sufficient data coverage to perform both one- and two-component fits across the range 30–500 d. For the rest of the sample, there is not enough data to determine the plateau onset and we only performed one-component fits between 150 and 500 d to find a single slope and y-intercept (s_2, b_2). For the objects where only the one-component fit was possible, we limited the phase range to 150–500 d because it is unclear whether these SNe display a plateau phase, and we want to ensure we do not include data before the transition onto the plateau. At least two data points were required per band per SN to perform the one-component fit.

On short time-scales, the photometric uncertainty dominates over the temporal evolution, which results in highly uncertain estimates of the slope. We therefore required at least two data points to be separated by at least 25 d, which reduced the number of SNe Ia with a measurement of the decline rate to 14. The minimum spacing of 25 d was determined by comparing the expected evolution with the expectation fluctuation within uncertainties. The mean uncertainty on the magnitude across our sample is 0.3 mag. The decline rate in the K_s band measured across the whole sample is 1.2 ± 0.2 mag /

100 d, meaning that a change of ~ 0.3 mag would be expected to occur across approximately 25 d.

We used reduced-χ^2 (χ^2_{red}) to describe the quality of a fit and we used the Akaike Information Criterion (AIC; Burnham & Anderson 2004) to determine the rank of the one- and two-component fits. AIC penalizes extra degrees of freedom to avoid overfitting the data, and is defined as follows:

$$AIC = -2\ln(L) + 2k,$$ (4)

where L is the likelihood and k is the number of free parameters. For comparing the one- and two-component models, we have $k = 2$, 4, respectively. Therefore, the two-component model is penalized for its two additional degrees of freedom by four AIC units. If the one- and two-component models differ by more than 2 AIC units, the model with a lower score was deemed the better fit. The best-matching value is taken from the 50th percentile, and the uncertainties were taken from the 16th and 84th percentiles of the marginalized distribution.

We used the best-matching fits to determine the properties of the plateau for each SN. The decline rate during the plateau phase is taken as the slope (s_2), which we quote in units of mag / 100 d. The average magnitude is calculated from b_2 and s_2 of the best-matching fit.

To minimize the impact from poorly sampled light curves, we also performed the one- and two-component fits for the full combined sample in absolute magnitude for each filter. Since there is minimal intrinsic scatter in the NIR, this should give a good estimate of the average decline rate for each filter.

3.2 SALT3 light curve fits

In order to determine the general properties of each SN, we fitted optical light curves taken from the literature with the package SNCOSMO, using the SALT3 model (Kenworthy et al. 2021). The sources of the optical light curves are listed in Table A1. For SNe with no published optical data, we used preliminary photometry from LCO provided by the Global Supernova Project (GSP). We excluded any UV or NIR data because SALT3 is not well trained at those wavelengths, and we restricted the data to between -10 d and $+40$ d. The SALT3 parameters derived from these fits (x_1, a metric of the light curve stretch, and c, a measure of the colour at peak) are presented in Table A1. There was no optical light curve available for SN 2013ct, so we were not able to derive SALT3 parameters.

3.3 Comparison to radiative transfer models

We compared our sample to the sub-M_{ch} SN Ia models of Shingles et al. (2022). These models use the Shen et al. (2018) model of a detonation of 1 $M_\odot$ WD and evolve the post-explosion composition using the radiative transfer code ARTIS. Earlier models by Fransson et al. (1996) predicted a strong decline in the optical as flux is redistributed to the NIR, which was not matched by observations. The improved treatment of non-local scattering and fluorescence by Fransson & Jerkstrand (2015) alleviated some of the discrepancies between the models and the observations, but no light curves were published for direct comparison. The models of Shingles et al. (2022) use a modified treatment of non-thermal energy deposition in which the the energy loss to free electrons is artificially boosted as a way to lower the ionization state. With this modification, the models are able to reconcile the strength of the [Fe II] features, which are generally underproduced by sub-M_{ch} models. Others have suggested that clumping of the ejecta is required to reduce the ionization state (Wilk, Hillier & Dessart 2018). The sub-M_{ch} model with a plasma

loss rate increased eight-fold (model 1) and is best able to reproduce the nebular NIR spectrum of the normal SN 2013ct (see fig. 6 in Shingles et al. 2022). In this work, we present a time-extended version of the sub-M_{ch}-heatboost8 model. For further details of the model, we refer the reader to Shingles et al. (2022). We also include the other three sub-M_{ch} models presented by Shingles et al. (2022) (sub-M_{ch}-heatboost×4, sub-M_{ch}, sub-M_{ch}-AxelrodNT), referred to from hereon as models 2, 3, and 4, respectively. However, because SN 2013ct is a normal SN Ia and is included in our sample, we focus on the best-matching model to its nebular spectrum (model 1). In Fig. 1, the model is scaled to the *J*-band photometry from our sample.

4 RESULTS

We constrain the onset of the plateau for a subset of SNe Ia in Section 4.1.1. In Sections 4.1.2 and 4.1.3, we present the decline rates and average magnitudes during the plateau of the SNe Ia in our sample. We compare the NIR plateau properties to SN properties at peak in Section 4.2.

4.1 Properties of the NIR plateau

We analyse the photometry presented in Section 2 and shown in Fig. 1 using three metrics: the onset of the plateau, the decline rate, and the average magnitude during the plateau. These metrics are derived from the fits either to each individual SN or to the sample as a whole in each filter, as described in Section 3.1.

4.1.1 Constraining the onset of the plateau

SNe 2001el, 2011fe, 2012ht, 2014J, 2018gv, 2021pit, and 2021aefx have data before and during the plateau, enabling us to constrain the phase of the onset of the plateau. The onset of the plateau is calculated by fitting a two-component linear fit to the light curves, as described in Section 3.1 and shown in Fig. 2. We also fit each SN with a one-component fit and compare the result to the two-component fit using the AIC. If the one- and two-component fits differ by more than two AIC units, the model with the lower AIC is deemed significantly better.

SN 2021pit, which is the best sampled SN along the transition onto the plateau, is best fit with two components in *J* and *H*, and yields $t_0^J = 130^{+30}_{-70}$ d and $t_0^H = 160^{+30}_{-40}$ d. The K_s band is best fit with a single-component decline (ΔAIC = 5). The uncertainty on the time of the onset of the plateau is large and we are unable to constrain the onset to the order of a few days, likely due to the gradual nature of the transition.

The results from the fits to SNe 2011fe, 2012ht, 2014J, 2018gv, and 2021aefx are summarized in Table 4. All *J*- and *H*-band light curves are best matched by a two-component model. Only SNe 2001el and 2021pit have sufficient K_s-band data to perform one- and two-component fits, and they were both best matched by a one-component model suggesting no plateau exists in this band.

We find that the t_0^J and t_0^H values for the other SNe are consistent with those derived for SN 2021pit. We note that SN 2012ht has pre-transition data in *F160W*, whereas the post-transition data is taken with *H*; therefore, the parameters derived describing the transition onto the plateau should be treated with caution. Similarly, SN 2021pit has post-transition data from *HST* in *F160W*. However, repeating the fit excluding the *HST* data produces consistent results ($t_0^H = 140 \pm 30$ d).

We calculate the weighted mean of t_0 for all measurements across one filter, taking into account the uncertainties, and find $t_0^J = 90 \pm 20$
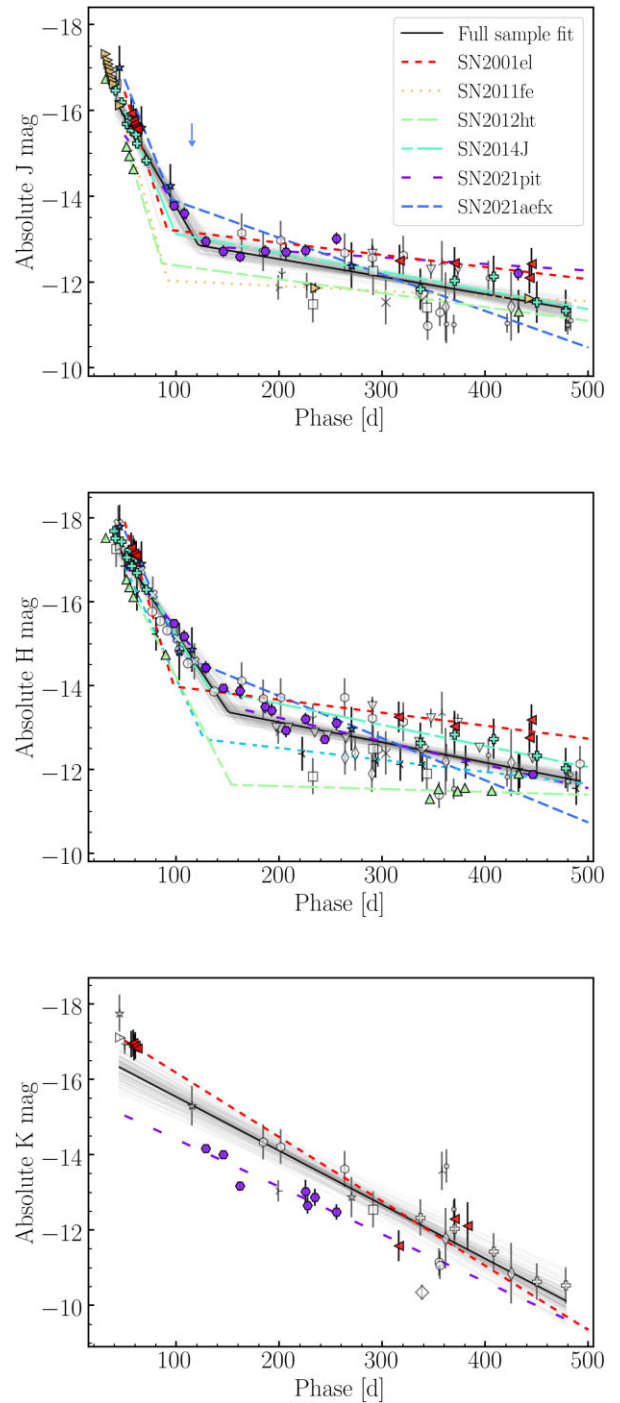

Figure 2. The observed light curves and two-component MCMC fits for the *J* (top), *H* (middle), and K_s (bottom) filters. The best fits (one- or two-component) to the NIR light curves of the whole sample are shown as black solid lines, with the various MCMC iterations shown as faded grey lines. Both the *J* and *H* bands have a non-zero decline rate but are consistent with zero within 2σ, and are best fit with two components. The decline rate in the K_s band is inconsistent with zero at a $>6\sigma$ confidence level, and is best matched by a one-component fit. We also show the best-matching fits to the SNe Ia with sufficient data (markers are the same as in Fig. 1).

Table 4. Summary of parameters for the fits performed for SNe Ia with data available before and after the transition onto the plateau. We perform both a one- and two-component fit to each light curve. SNe Ia with a maximum separation of less than 25 d between data points are not included (see Section 4.1.2).

SN	Filter	s_1 [mag/100 d]	s_2 [mag/100 d]	t_0 [d]	χ^2_{red} One-comp.	χ^2_{red} Two-comp.	ΔAIC
(1)	(2)	(3)	(4)	(5)	(6)	(7)	(8)
Full sample	J	$5.2^{+0.9}_{-0.5}$	0.4 ± 0.1	120 ± 10	29	14	1137
Full sample	H	$3.5^{+0.3}_{-0.3}$	0.5 ± 0.1	140 ± 10	63	29	3832
Full sample	K_s	–	1.2 ± 0.4	–	33	42	-407
SN 2000cx	J	–	-0.1 ± 0.1	–	0.1	–	–
SN 2000cx	H	–	-0.2 ± 0.1	–	0.2	–	–
SN 2001el	J	$7.9^{+5.9}_{-4.6}$	0.3 ± 0.2	90^{+40}_{-50}	0.7	0.08	2
SN 2001el	H	$8.3^{+7.1}_{-4.9}$	0.3 ± 0.3	100^{+40}_{-50}	1.2	0.2	4
SN 2001el	K_s	–	1.7 ± 0.1	–	1.2	1.7	-4
SN 2003hv	H	–	0.1 ± 0.3	–	0.03	–	–
SN 2011fe	J	8.8 ± 0.5	0.1 ± 0.5	90 ± 3	80	0.1	790
SN 2012ht	J	7.9 ± 0.2	0.3 ± 0.3	90 ± 10	274	0.1	1093
SN 2012ht*	H	$4.9^{+0.3}_{-0.2}$	0.1 ± 0.1	150 ± 10	230	4	1113
SN 2013aa	J	–	0.3 ± 1.2	–	0.1	–	–
SN 2013aa	H	–	0.3 ± 1.2	–	0.01	–	–
SN 2013aa	K_s	–	$0.8^{+1.1}_{-1.4}$	–	0.2	–	–
SN 2014J	J	5.7 ± 0.3	0.4 ± 0.3	100 ± 20	17	1	213
SN 2014J	H	4.1 ± 0.4	0.5 ± 0.3	130 ± 40	8	2	81
SN 2014J	K_s	–	$1.3^{+0.1}_{-0.2}$	–	0.06	–	–
SN 2017erp	J	–	0.5 ± 0.4	–	0.1	–	–
SN 2017erp	H	–	0.5 ± 0.4	–	0.01	–	–
SN 2018gv	F160W	$5.4^{+1.8}_{-1.7}$	0.3 ± 0.2	130^{+20}_{-30}	4	0.1	31
SN 2020uxz	J	–	$0.1^{+0.9}_{-0.3}$	–	0.001	–	–
SN 2020uxz	H	–	$0.0^{+0.9}_{-0.4}$	–	0.001	–	–
SN 2021jad	J	–	0.3 ± 0.1	–	0.1	–	–
SN 2021jad	H	–	0.5 ± 0.1	–	0.1	–	–
SN 2021jad	K_s	–	0.9 ± 0.4	–	0.01	–	–
SN 2021pit	J	$3.1^{+1.7}_{-0.7}$	0.2 ± 0.1	130^{+30}_{-70}	6	2	40
SN 2021pit*	H	$3.5^{+3.5}_{-0.6}$	0.6 ± 0.1	160^{+30}_{-40}	10	4	50
SN 2021pit	K_s	–	$1.3^{+0.2}_{-0.3}$	–	4	6	-5
SN 2021aefx	J	$6.0^{+2.9}_{-2.5}$	0.9 ± 0.5		2.5	0.3	3
SN 2021aefx	H	$5.2^{+2.5}_{-1.8}$	$1.0^{+0.5}_{-0.6}$	100^{+60}_{-50}	2	0.2	3
SN 2021aefx	K_s	–	$1.6^{+0.3}_{-0.5}$	–	0.01	–	–
SN 2021wuf	H	–	$1.1^{+1.1}_{-1.0}$	–	0.1	–	–

Notes. Columns (3) and (4): s_1 and s_2 are the slopes prior to and during the plateau. We also include s_2 for SNe Ia that exclusively have data during the plateau, for which we performed only one-component fits. Column (5): t_0 is the phase at which the SN transitions onto the plateau. Columns (6) and (7): χ^2_{red} values of the one- and two-component fits, describing the quality of the best-matching fit. Columns (8): The difference between the AIC values for the one- and two-component fits (ΔAIC = AIC$_{one-comp.}$ $-$ AIC$_{two-comp.}$). If the AIC values of two models differ by more than two units, the model with the lower AIC value is deemed significantly better, and the parameters for that model are quoted.
* The pre- and post-transition data have contributions from both space- and ground-based telescopes.

d and $t_0^H = 130 \pm 20$ d, where the uncertainties are quoted as the standard deviations. This implies t_0^J and t_0^H are consistent. This disagrees with the trend for the secondary maximum, where the second peak occurs in *H* before it occurs in *J* (Kasen 2006; Dhawan et al. 2015). However, a larger, better sampled collection of SNe is required to reduce the uncertainties on the time of the transition and test if the time of transition is truly consistent between the *J* and *H* bands.

To increase the sample size, we repeat the same one- and two-component fits for the full combined sample (Fig. 2). We find that the *J*- and *H*-band data are best fit with two components (ΔAIC = 1137 and 3832), with $t_0^J = 120 \pm 10$ d and $t_0^H = 140 \pm 10$ d.

The K_s band is best fit with a single, constantly declining component (ΔAIC = 580).

4.1.2 Decline rate during the plateau

In Fig. 2 we show two-component linear fits, fitted to all the SNe Ia simultaneously in absolute magnitude in each filter. By fitting the full combined sample, the influence from a single, potentially poorly sampled SN, is minimized. In the *J* and *H* bands, the decline rates of the second component (during the plateau) are $s_2^J = 0.4 \pm 0.1$ and $s_2^H = 0.5 \pm 0.1$ mag / 100 d, respectively. These are inconsistent with
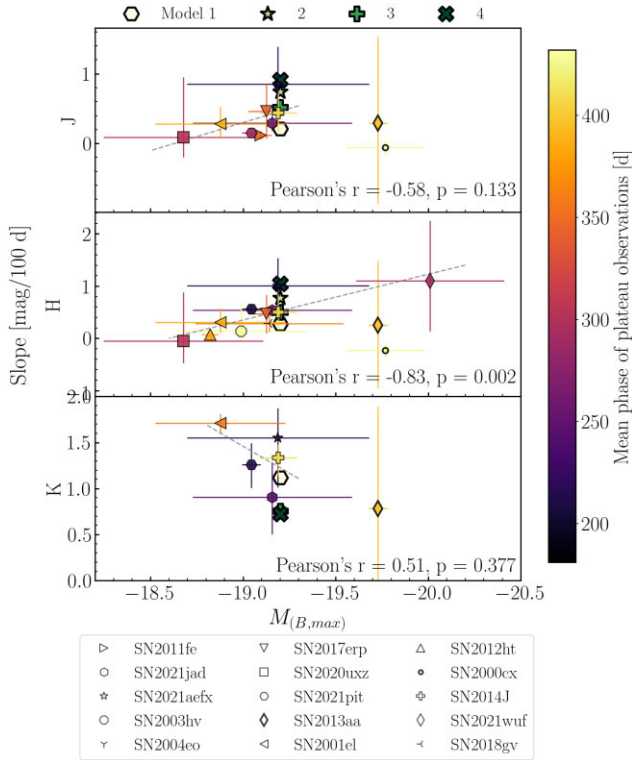
Figure 3. The measured decline rate as a function of M_{max}^B for the J (top), H (middle), and K_s (bottom) filters. The marker colour represents the mean phase of the observations. We include the predictions from the sub-M_{ch} models presented by Shingles et al. (2022), using -19.2 as M_{max}^B from Shen et al. (2018). The dashed line shows a linear fit to the sample, excluding SNe 2013aa and 2000cx, which are considered as outliers and are highlighted by a thicker marker edge. We also show the Pearson r-coefficient and the corresponding p-values. A significant correlation ($p < 0.05$) is identified in the H band.

zero at a $>3\sigma$ confidence level, meaning that the decline does not cease completely during the plateau. However, by comparing to the decline rate prior to the plateau ($s_1^J = 4.3 \pm 0.6$ and $s_1^H = 3.6_{-0.3}^{+0.4}$ mag / 100 d) it is clear that the decline slows significantly. The decline rate in K_s is inconsistent with zero at a $>6\sigma$ confidence level, since this band is best fit by a single component with a continuous decline ($s_2^K = 1.2 \pm 0.2$ mag / 100 d).

In Fig. 3, we show the decline rate for each individual SN as a function of the absolute B-band magnitude at peak (M_{max}^B) and the mean phase of the observations. In the J band, most SNe Ia have a slope consistent with zero. The decline rate averaged across the SNe Ia in the J band is 0.4 ± 0.4 mag / 100 d, where the uncertainty is the standard deviation weighted by the individual uncertainties. In the H band, the average decline rate is 0.5 ± 0.3 mag / 100 d. The K_s band behaves differently from the other two bands, with an average decline rate of 1.3 mag / 100 d and a weighted standard deviation of 0.3 mag / 100 d.

When comparing the decline rates between J and H for each SN Ia in the sample, they are consistent for six SNe Ia. One SN Ia has a steeper decline in J, whilst two have a steeper decline in H. Those with a steeper decline in the H band have observations limited to <250 d, whereas those with a consistent decline rate, or shallower decline rate in H, have observations taken later than 250 d. This points to an evolution in the decline rate in the H band across the plateau, with a steeper initial decline in H, which levels off with time. This evolution
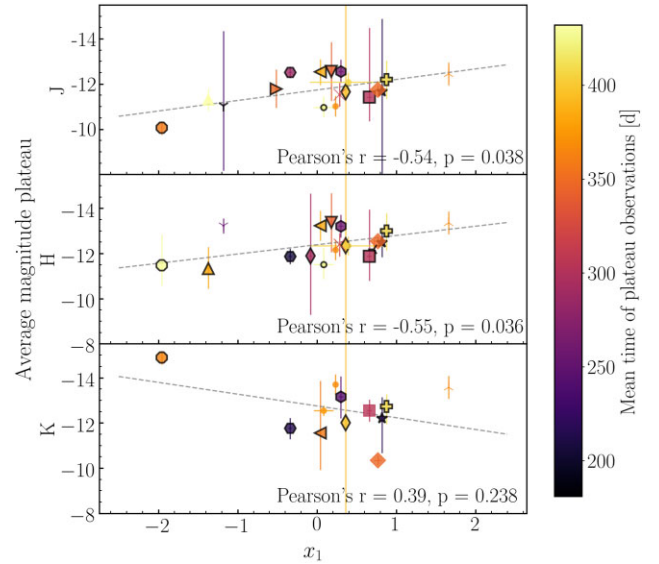

Figure 4. The average magnitude measured for each SN Ia during the plateau as a function of x_1, with the colour indicating the mean phase of the observations, for the J (top), H (middle), and K_s (bottom) bands. We include measurements taken from a single data point (shown as markers without a black outline), which should give a reasonable estimate of the magnitude in the flatter J and H bands, but should be interpreted with caution for the K_s band due to its steeper evolution throughout the plateau. We perform a linear fit (dashed line) in each filter and include the calculated Pearson's r-coefficient and the corresponding p-value. We find a significant ($p < 0.05$) trend of the average magnitude during the plateau with x_1 in the J and H bands.

was also apparent in the well-sampled light curves of SN 2017erp and SN 2018gv (Graur et al. 2020), where at the start of the plateau phase the decline rate decreases, but near the end of the plateau phase the decline rate begins to rise again. Unfortunately, no well-sampled J-band light curve is available for comparison, but we refer the reader to Appendix B for an analysis of this evolution for model 1.

4.1.3 Average magnitude during the plateau

In Fig. 4, we show the average magnitude as a function of the light curve stretch (x_1), as well as the mean phase during which the data were taken. SNe Ia with only a single data point during the plateau are included but are indicated by markers without a black outline. For the J and H bands a single data point should give a reliable estimate of the average magnitude during the plateau due to the approximately flat decline rate in these two filters. However, the K_s band estimates for these SNe Ia are more uncertain due to the steeper decline in this filter.

4.2 Correlations between plateau properties and SN properties at peak

Graur et al. (2020) find that the average magnitude during the plateau in the H band scales with $\Delta m_{100}(H)$ (the decrease in magnitude between peak and 100 d after peak in the H band) and $\Delta m_{15}(B)$. In the following section, we explore the correlations between the plateau properties, M_{max}^B, c, and x_1 (available in Table A1).

To measure how strongly two variables are linearly related, we use Pearson's correlation coefficient, r. The significance of the correlation is measured by the p-value, with $p < 0.05$ indicating a statistically significant correlation. We find a significant correlation between x_1 and the average J- and H-band magnitudes during the

plateau ($r = -0.54$, -0.55, and $p = 0.038$ and 0.036, respectively), implying that SNe Ia with broader light curves (larger x_1 values) are intrinsically brighter in J and H during the plateau (Fig. 4). This trend agrees with the correlation found by Graur et al. (2020) for the H band. We find no statistically significant correlation between the average magnitude during the plateau and x_1 in the K_s band.

The average magnitude during the plateau is driven predominantly by the slope of the decline prior to the transition onto the plateau, a metric that can be approximated by $\Delta m_{100}(H)$, as shown by Graur et al. (2020). $\Delta m_{100}(H)$ shows a weak correlation with $\Delta m_{15}(B)$, as shown in fig. 3 of Graur et al. (2020). Combining these results from Graur et al. (2020) and this work, we suggest that broader SNe Ia (larger x_1, smaller $\Delta_{15}(B)$) tend to decline less in the period 100 days after maximum in H and therefore have a higher average magnitude during the plateau phase.

One potential source of bias worth considering is that the likelihood of being able to observe a SN Ia during the plateau is a function of its brightness on the plateau. If a SN Ia has a shallower decline after maximum (smaller $\Delta m_{100}(H)$), it will remain brighter during the plateau. Therefore, it is likely that studies of SNe Ia on the plateau are inherently biased and tend to sample the SNe Ia that are brighter during the plateau and lie at the lower end of the $\Delta m_{100}(H)$ population.

We find no significant correlations between the slope during the plateau and M_{max}^B, x_1, or c. However, we note that SNe 2000cx and 2013aa are clear outliers in M_{max}^B versus slope (Fig. 3). We check for a linear correlation between the slope and M_{max}^B excluding these two SNe Ia. The result from this fit is shown as the dashed line in Fig. 3. This correlation is significant in H with Pearson's r coefficient $= -0.83$ and p-value $= 0.002$, implying that SNe Ia that are more luminous at peak tend to decline faster during the plateau phase. It is unclear why SNe 2000cx and 2013aa do not follow this trend, but both are very luminous at peak ($M_{max}^B < -19.5$). We discuss these objects in more detail in Section 5.3.

The timing of the secondary maximum of SNe Ia shows a strong correlation with the stretch of the light curve (Dhawan et al. 2015; Papadogiannakis et al. 2019), with narrow, fast evolving SNe Ia having an earlier secondary maximum. An increase in the total mass of ^{56}Ni (corresponding to a smaller $\Delta m_{15}(B)$) delays the onset of the secondary maximum due to the higher temperature of the ejecta (Kasen 2006). We suggest that the NIR plateau is caused by a similar mechanism as the secondary maximum, and we expect similar correlations to hold for the NIR plateau. The timing of the onset of the plateau could therefore be expected to correlate with the stretch of the light curve. We test whether there is any correlation between x_1 and the t_0 values calculated in Section 4.1.1 and find no statistically significant correlations (p-values $= 0.8$ and 0.1 for the J and H bands, respectively). However, for most SNe the phase of the onset is very poorly constrained due to poor sampling, and we cannot rule out a possible correlation between these parameters. Future studies of SNe Ia with higher cadence observations (< 20 d) around the transition phase (70–150 d) will help to answer this question.

5 DISCUSSION

In Section 5.1, we provide a theoretical discussion of the NIR spectral evolution. We then answer the questions raised by Graur et al. (2020): 'Is there a plateau in the K_s band'? and 'Does the H-band plateau consist of two distinct branches'?, by analysing the results presented in Section 4. We discuss how the models presented in Section 3.3 compare to our observations in Section 5.2. In Section 5.3, we discuss the peculiar SN Ia sub-types present in the sample and compare their behaviour on the plateau to the normal SNe Ia.

5.1 Relating the photometric evolution to spectral features

The NIR spectrum during the plateau contains many forbidden iron group lines. We show the spectral evolution of SN 2014J throughout the plateau in Fig. 5, with the main spectral features indicated (these spectra were previously published by Dhawan et al. 2018 and Diamond et al. 2018). The strength of the lines at 1.54 μm, 1.74 μm (H band), 2.02 μm, 2.15 μm, 2.22 μm, and 2.35 μm (K_s band) decrease with time. These lines contain emission features coming from [Co II], [Co III], [Fe II], and [Fe III], although from Fig. 5 alone it is not possible to say which emission lines from which elements dominate each feature.

To learn more about the individual contributions to each emission feature, we use information about the transition probability of each line from the atomic data made available by the National Institute of Standards and Technology (NIST).[4] The transitions are optically thin, so their fluxes are proportional to their upper-level population times their emission probability. The upper-level populations will be similar if their excitation energies are similar; they have similar statistical weights ($g = 2J + 1$, where g is the statistical weight and J is the quantum number representing the combined total angular momentum of the electron), and they are both metastable states (only forbidden downward transitions). Therefore, we use the ratios of transition probabilities as a proxy for line strength ratios if the emission lines originate from the same species and have similar excitation energies for the upper level (Jerkstrand et al. 2015).

The two [Co III] features in the J band (1.27 μm and 1.31 μm) and the two [Co III] features in the H band (1.54 μm and 1.74 μm) all have similar upper energy levels (23 060.95, 23 060.95, 23 435.93, and 22 721.42 cm^{-1}, respectively). The 1.27 μm and 1.31 μm lines originate from the same a^4P multiplet, but come from states with $J = 5/2$ and $J = 3/2$, respectively, meaning that the 1.27 μm feature is expected to be about $(5+1)/(3+1) = 1.5$ times stronger. The 1.54 μm and 1.74 μm lines come from the same upper state ($a^2G_{9/2}$), so the A_{ki} ratio provides a reliable estimate of the flux ratio of these two lines. The emission line at 1.54 μm has the highest transition probability ($A_{ki} = 1.3 \times 10^{-1}$ s^{-1}), whereas the lines in the J band have transition probabilities of 5.4×10^{-3} and 2.5×10^{-3} s^{-1}, respectively. The line at 1.74 μm has a transition probability of 4.2×10^{-2} s^{-1}. The dominant [Co III] features therefore sit in the H band, and this band will be most impacted by the decay from ^{56}Co $\rightarrow$ ^{56}Fe.

The [Fe III] features at 2.15, 2.22, and 2.35 μm in the K_s band have similar upper energy levels (25 142.12, 24 558.44, and 24 558.44 cm^{-1}, respectively), all originate from ^3G, have comparable transition probabilities ($A_{ki} = 3.4 \times 10^{-2}$, 3.20×10^{-2}, and 2.25×10^{-2} s^{-1}), but come from different states ($J = 4$, 6, 5, respectively) meaning that the feature at 2.22 μm is the strongest of the three.

The features in the J band show only limited decay with time relative to the H band, which aligns with the lower transition probabilities of the [Co III] features at these wavelengths. This is further supported by Fig. 6, which deconstructs the spectrum of model 1 to show the contributions from different species. This is likely not the only correct model for all SNe Ia, but it demonstrates the commonly identified features whilst also being able to model the plateau behaviour. The model suggests that the J band is dominated by [Fe II], whereas the H band has significant contribution from [Co III]. The feature at 1.74 μm is composed of three emission lines from [Fe II], [Fe III], and [Co III]. The feature at 1.74 μm is dominated

---

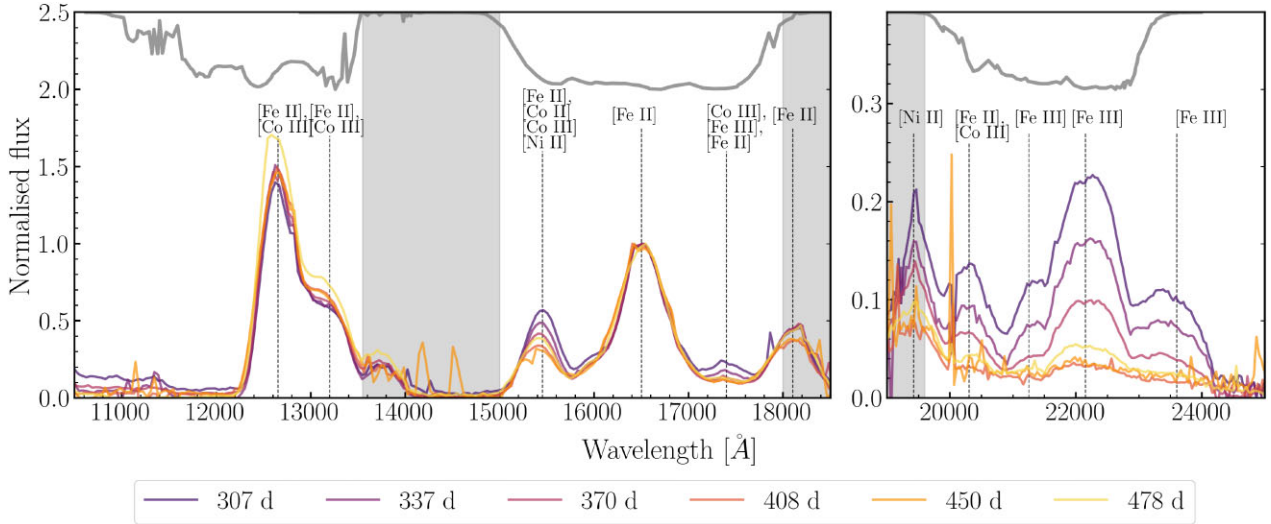[4] https://physics.nist.gov/PhysRefData/ASD

Figure 5. NIR spectral series of SN 2014J, covering 307–478 d. *Left:* The wavelength range covering the *J* and *H* bands. *Right:* The K_s-band spectrum (note the different range on the y-axis). The key spectral features are marked, and the telluric regions are indicated by grey regions. The flux has been normalized to the [Fe II] feature at 1.65 μm. The grey solid curves show the 2MASS *J*, *H*, and K_s filter response functions.
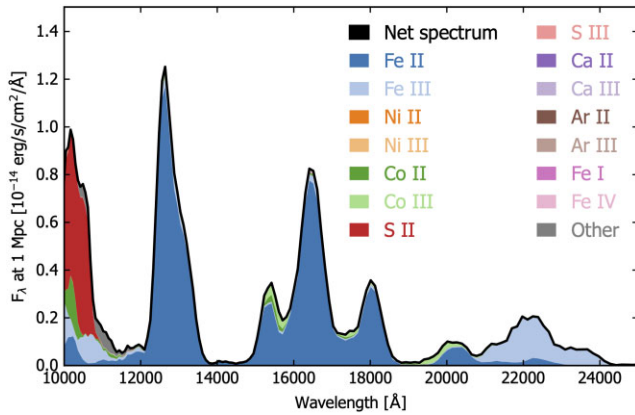

Figure 6. Figure adapted from Shingles et al. (2022) with showing the contribution from each species to the sub-M_{ch} heatboost8 spectrum at 247 d. Most of the *J* and *H* bands are dominated by [Fe II], with some [Co III] contributions in the *H* band. The K_s band is dominated by [Fe III] emission.

by [Fe II], but the model demonstrates that it also has significant contribution from [Co III], explaining its decay with time. This is in agreement with previously identified features in SNe Ia. The K_s band is dominated by [Fe III] features (see Fig. 6).

5.1.1 Is there a plateau in the K_s band?

Graur et al. (2020) speculated that based on the synthetic photometry of SN 2014J, the NIR plateau does not extend to the K_s band. In Section 4, we presented additional data in the K_s band supporting this conclusion. Here, we rationalize the lack of a plateau in the K_s band by referencing the spectroscopic evolution of SN 2014J as a representative of a normal SN Ia (see Fig. 5).

As shown in Figs 5 and 6, the *K*-band is dominated by an [Fe III] complex, whereas the *J* and *H* bands are dominated by [Fe II] features (Diamond et al. 2018; Shingles et al. 2022). Throughout the plateau phase, the strength of [Fe III] features decreases, whereas [Fe II] features remain constant, suggesting that doubly ionized iron ions

are recombining to singly ionized iron. Since there is no contribution of [Fe II] in the K_s band, the flux continues to decline following the recombination rate of [Fe III].

5.1.2 Are there two branches in the H-band plateau?

Graur et al. (2020) find two clusters in the average magnitude of the *H* band, corresponding to a more luminous branch and a faint branch. We note that the photometry in fig. 2 in Graur et al. (2020) is scaled to M_{max}^H, whereas the photometry in Fig. 1 is not scaled because *H*-band data around peak is not available for all the SNe Ia in our sample. A direct comparison between the plots is therefore not possible, but we note that the *H*-band data in this paper is not separated into two different branches. This could mean that the magnitudes of the plateau in the *H* band make up a continuous distribution, but only the extremes of this population were sampled by Graur et al. (2020).

We test this first explanation by comparing the average *H*-band magnitudes on the plateau of the SNe Ia presented by Graur et al. (2020) to the additional SNe Ia presented in this paper (Fig. 7). The gap between −11.5 and −12.5 mag found by Graur et al. (2020) is populated by the SNe Ia presented in this paper, suggesting that the *H*-band magnitudes on the plateau represent a continuous distribution. A simple Kolmogorov-Smirnov (KS) test enables us to test whether the two samples are likely sampled from the same distribution. We find a KS-value = 0.4 and *p*-value = 0.5, suggesting that the two samples are most likely drawn from the same population.

Despite not seeing two separate branches in the *H*-band plateau, the behaviour in the *H* band is less homogeneous than in the *J* band. Fig. 5 shows a strong [Fe II]/[Co II]/[Co III] complex present in the *H* band, which is dominated by [Fe II] and [Co III]. This feature decreases in strength throughout the plateau due to the continued decay of ^{56}Co to ^{56}Fe (Childress et al. 2015; Flörs et al. 2018), which would suggest that there should be some decrease in flux in the *H* band during the plateau phase. This aligns well with the model predictions, which suggest that the *J* band decays slower during the plateau phase than the *H* band. We would expect the decline rate in the *H* band to flatten with time, as the relative contribution of the [Co III] feature decreases and the decay of these features will
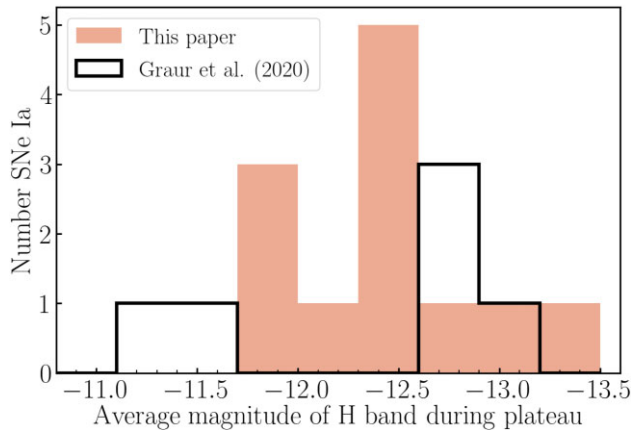
Figure 7. A histogram comparing the average magnitude of the plateau in the *H* band between Graur et al. (2020) and this paper. Graur et al. (2020) noticed bimodal behaviour in the average magnitudes of the *H* band, but the additional data presented in this paper suggests the *H*-band magnitudes represent a continuous distribution.

have a smaller overall impact on the integrated flux across the filter. Generally, the SNe Ia with observations taken at later phases have shallower declines (with the exception of SN 2020uxz), suggesting that the variation seen in the *H* band could be driven by whether the observations are taken during the early or late stages of the plateau.

5.2 Comparing models to the observations

The light curve of model 1 is shown in Fig. 1, where it is scaled to the *J*-band photometry of our sample, the wavelength range best matched by the model presented by Shingles et al. (2022). In the *H* and K_s bands, the model underpredicts the magnitude. In the *H* band, the discrepancy is greatest near the beginning of the plateau but lessens with time, whereas in the K_s band the offset remains constant. This mismatch between the relative model flux and observed flux in each band is likely due to specific spectral features not being reproduced as well by the models. Fig. 6, which is an extended version of fig. 5 from Shingles et al. (2022), highlights that the *J* band is dominated by an [Fe II] complex spanning 1.22–1.36 μm. The *H* band contains a complex of [Fe II], [Fe III], [Co II], and [Co III]. Fig. 5 in Shingles et al. (2022), which compares the model spectrum to the spectrum of SN 2013ct, demonstrates that the model is able to reproduce most spectral features across the *J* and *H* bands. However, the feature at 1.54 μm, which is dominated by [Fe II] in Fig. 6, is underestimated. This feature also has contributions from [Fe III], [Co II], and [Co III], which may be underestimated by model 1.

In Fig. 3, we show the average decline rate of model 1 on the plateau, between 150 and 500 d. We find ~0.2, 0.3, and 1.1 mag / 100 d in the *J*, *H*, and K_s bands, respectively. This is in agreement with the observational data regarding the presence of the plateau in the *H* and *J* bands, as well as the lack of a plateau in the K_s band. Moreover, the decline rate predicted by model 1 sits in the parameter space defined by our sample. Fig. 3 also shows the average decline rates for the other three sub-M_{ch} models. All four models fall within the parameter space set by the observed SNe Ia, although in the *J* and *H* bands, models 2, 3, and 4 tend to predict steeper declines than the majority of our sample (with the exception of SN 2021wuf). We provide a more detailed analysis of the magnitude evolution of model 1 in Appendix B, including an analysis of the first and second

derivatives, to characterize the evolution of the slope as well as the inflection points.

5.3 Peculiar SN Ia subtypes on the plateau

The majority of the SNe Ia presented in this paper are classified as 'normal' SNe Ia based on their maximum-light spectra (see Table A1), although there are a few exceptions. SN 2021wuf is classified as a 91T-like SN Ia, a subclass that follows the width–luminosity relation (Rust 1974; Pskovskii 1977; Phillips, Phillips & M. 1993) and is used for cosmology, but with light curves that are generally brighter and slower evolving than normal SNe Ia. They show a preference for exploding in late-type galaxies (Taubenberger 2017). SN 2000cx is a peculiar SN Ia, with properties similar to the 91T-like sub-class but with an asymmetric *B*-band light curve and a peculiar colour evolution (Li et al. 2001). SNe 2004eo and 2012ht are classified as transitional objects between normal and sub-luminous SNe Ia (Yamanaka et al. 2014). Whether these transitional SNe Ia should be used for cosmology is an on-going debate (Burns et al. 2018; Gall et al. 2018; Dhawan et al. 2022, Harvey et al., in preparation).

SNe 2000cx, 2012ht, and 2021wuf all have consistent average magnitudes in *H* during the plateau and follow the trend that narrower SNe Ia tend to be fainter during the plateau. SN 2004eo sits above this trend in *H*, being more luminous than expected for its measured x_1. However, in *J*, SN 2004eo is consistent with this trend.

We found a correlation between M^B_{max} and the slope, and whilst the low decline rate of SN 2012ht fits into this trend, SN 2000cx is a clear outlier (Fig. 3). SN 2013aa, whilst being classified as a normal SN Ia, is also exceptionally luminous and similarly falls outside this correlation. On the other hand, SN 2021wuf shows a steep decline during the plateau, as expected from the correlation, although we note that this measurement is based on only two data points separated by 26 d (a minimum of 25 d is required to calculate a reliable slope). SN 2004eo only has two data points in *J*, and these are not sufficiently spaced to calculate a decline rate.

A larger sample is required to investigate these trends, but if overluminous SNe Ia tend to have a flatter plateau in *J* and *H*, this may imply that there is an additional spectral contribution at these wavelengths supporting their luminosity for a longer period.

It has been suggested that the single-degenerate scenario with a near-M_{ch} WD could be solely responsible for overluminous 91T-like SNe Ia rather than the normal SN Ia population (Childress et al. 2015; Fisher & Jumper 2015; Byrohl, Fisher & Townsley 2019). Previous studies have also found that overluminous 91T-like SNe Ia show flux excesses at a higher rate than normal SNe Ia, which could point towards interaction with a non-degenerate companion in the single-degenerate scenario (Jiang et al. 2018; Deckers et al. 2022, but see Burke et al. 2022 for an alternative view).

6 CONCLUSIONS

We present NIR photometry of 24 SNe Ia during the plateau phase. From this extensive data set, we are able to measure the average magnitude and slope of the plateau in *J*, *H*, and K_s. We compare these plateau properties to the properties at maximum light and find a significant correlation between x_1 and the magnitude of the plateau in *J* and *H*, as well as between M^B_{max} and the slope in *H*. From these correlations, we conclude that the main driving factor for the magnitude of the plateau is the luminosity at maximum light, which, in turn, correlates with the decline in magnitude in *H* 100 d after maximum, ($\Delta m_{100}(H)$). SNe Ia which are more luminous at peak appear to decline faster during the plateau, although there are

clear outliers to this trend. Specifically, the overluminous SNe in our sample behave differently from the normal SNe Ia during the plateau. Overluminous SNe Ia appear to decline slower than predicted by the trend found between M_{max}^B and the slope, which could imply that there is an additional spectral contribution during the plateau.

We constrain the onset of the plateau to 70–150 d. The secondary maximum occurs in H before it occurs in J (Kasen 2006; Dhawan et al. 2015), but due to the large uncertainties in our estimates of the transition phase we are unable to determine if this is the case for the plateau. We expect a correlation to exist between the time of the onset of the plateau and the peak luminosity of a SN Ia, akin to the correlation found for the secondary maximum, but this could not be confirmed for our sample.

We compare our photometry to models produced by Shingles et al. (2022) and find good agreement regarding the evolution during the plateau, albeit the models underpredict the luminosity in H and K_s. However, the best-matching model has reduced non-thermal ionization rates that leads to lower ionization states, but no physical justification for reducing these rates has yet been proposed.

An analysis of six spectra of SN 2014J taken throughout the plateau enables us to explain the presence of the plateau in J and H, as well as the absence of the plateau in K_s. The dominant [Fe II] features that remain constant throughout the plateau sit in the J and H bands, whilst the K_s band hosts mainly [Fe III] features, which recombine to [Fe II] during the plateau phase.

A very limited number of SNe Ia have NIR coverage during the onset of the plateau. Extending this parameter space by obtaining higher cadence observations (< 20 d) around the transition phase (70—150 d) will enable us to test whether the timing of the plateau correlates with the magnitude at peak, as is the case for the secondary maximum, although we note that this is often difficult due to visibility constraints from the ground. We strongly encourage follow-up of overluminous SNe Ia to test whether they all decline faster during the plateau than expected, since this might imply these events have a different origin. Finally, obtaining more UV photometry coeval with NIR photometry would enable us to determine if flux truly is being redistributed from the UV to the NIR.

ACKNOWLEDGEMENTS

DATA AVAILABILITY

All the photometry presented in this paper is made available in machine-readable format in the supplementary material.

REFERENCES

Ahn C. P. et al., 2014, ApJS, 211, 17
Anderson J. P. et al., 2014, ApJ, 786, 67
Avelino A., Friedman A. S., Mandel K. S., Jones D. O., Challis P. J., Kirshner R. P., 2019, ApJ, 887, 106
Axelrod T. S., 1980, PhD Thesis, UCSC
Bailer-Jones C. A. L., Bizenberger P., Storz C., 2000, SPIE, 4008, 1305
Barbary K. et al., 2022, Astrophysics Source Code Library, record ascl:1611.017
Barone-Nugent R. L. et al., 2012, MNRAS, 425, 1007
Baumeister H. et al., 2003, SPIE, 4841, 343
Botyánszki J., Kasen D., 2017, ApJ, 845, 176
Brennan S. J., Fraser M., 2022, A&A, 667, A62
Brown T. M. et al., 2013, PASP, 125, 1031
Brown P. J. et al., 2019, ApJ, 877, 152
Burke J., Howell D. A., Sand D. J., Hosseinzadeh G., 2022, preprint (arXiv:2208.11201)
Burnham K. P., Anderson D. R., 2004, Sociol. Meth. Res., 33, 261
Burns C. R. et al., 2018, ApJ, 869, 56
Burns C. R. et al., 2020, ApJ, 895, 118
Byrohl C., Fisher R., Townsley D., 2019, ApJ, 878, 67
Childress M. J. et al., 2015, MNRAS, 454, 3816
Clark P., Maguire K., Bulla M., Galbany L., Sullivan M., Anderson J. P., Smartt S. J., 2021, MNRAS, 507, 4367
Deckers M. et al., 2022, MNRAS, 512, 1317
Dhawan S., Leibundgut B., Spyromilio J., Maguire K., 2015, MNRAS, 448, 1345
Dhawan S., Flörs A., Leibundgut B., Maguire K., Kerzendorf W., Taubenberger S., Van Kerkwijk M. H, Spyromilio J., 2018, A&A, 619, A102
Dhawan S. et al., 2022, ApJ, 934, 185
Diamond T. R. et al., 2018, ApJ, 861, 119
Djupvik A. A., Andersen J., 2010, in Diego J., Goicoechea L., González-Serrano J., Gorgas J., eds, Highlights of Spanish Astrophysics V, Ap&SS Proc.. SPIE, Bellingham, p. 211

Eikenberry S. et al., 2008, in McLean I. S., Casali M. M., eds, Proc. SPIE Conf. Ser. Vol. 7014, Ground-based and Airborne Instrumentation for Astronomy II. SPIE, Bellingham, p. 70140V

Elias J. H., Frogel J. A., Tololo C., Observatory I.-A., Hackwell J. A., Persson S. E., Wilson M., Campanas L., 1981, ApJL, 251, L13

Elias J. H., Matthews K., Neugebauer G., Persson S. E., Elias J. H., Matthews K., Neugebauer G., Persson S. E., 1985, ApJ, 296, 379

Filippenko A. V. et al., 1992, AJ, 104, 1543

Fisher R., Jumper K., 2015, ApJ, 805, 150

Flewelling H. A. et al., 2020, 7 ApJS, 251

Flörs A., Spyromilio J., Maguire K., Taubenberger S., Kerzendorf W. E., Dhawan S., 2018, A&A, 620, A200

Flörs A. et al., 2020, MNRAS, 491, 2902

Foreman-Mackey D., Hogg D. W., Lang D., Goodman J., 2013, PASP, 125, 306

Fransson C., Jerkstrand A., 2015, ApJL, 814, L2

Fransson C., Houck J., Kozma C., 1996, in Proc. of the IAU Colloq. 145. p. 211

Galbany L. et al., 2022, priprint (arXiv:2209.02546)

Gall C. et al., 2018, A&A, 611, A58

Graham M. J. et al., 2019, PASP, 131, 078001

Graur O. et al., 2020, Nat. Astron., 4, 188

Green G. M., 2018, J. Open Source Softw., 3, 695

Hamuy M. et al., 2003, Nature, 424, 651

Hillebrandt W., Kromer M., Röpke F. K., Ruiter A. J., 2013, Front. Phys., 8, 116

Hodapp K.-W. et al., 2003, SPIE, 4841, 869

Hosseinzadeh G. et al., 2017, ApJ, 845, L11

Jacobson-Galán W. V., Dimitriadis G., Foley R. J., Kilpatrick C. D., 2018, ApJ, 857, 88

Jensen J. B., Tonry J. L., Barris B. J., Thompson R. I., Liu M. C., Rieke M. J., Ajhar E. A., Blakeslee J. P., 2003, ApJ, 583, 712

Jerkstrand A. et al., 2015, MNRAS, 448, 2482

Jha S. W., Maguire K., Sullivan M., 2019, Nat. Astron., 3, 706

Jiang J., Doi M., Maeda K., Shigeyama T., 2018, ApJ, 865, 149

Johansson J. et al., 2021, ApJ, 923, 237

Jones D. O. et al., 2022, ApJ, 933, 172

Kasen D., 2006, ApJ, 649, 939

Kenworthy W. D. et al., 2021, ApJ, 923, 265

Kollmeier J. A. et al., 2019, MNRAS, 486, 3041

Könyves-Tóth R. et al., 2020, ApJ, 892, 121

Kovács Z., Mall U., Bizenberger P., Baumeister H., Röser H.-J., 2004, in Garnett J. D., Beletic J. W., eds, Proc. SPIE Conf. Ser. Vol. 5499, Optical and Infrared Detectors for Astronomy. SPIE, Bellingham, p. 432

Krisciunas K. et al., 2003, AJ, 125, 166

Krisciunas K., Phillips M. M., Suntzeff N. B., 2004, ApJ, 602, L81

Leibundgut B. et al., 1993, AJ, 105, 301

Leloudas G. et al., 2009, A&A, 505, 265

Leonard D. C., 2007, ApJ, 670, 1275

Li W. et al., 2001, PASP, 113, 1178

Lundqvist P. et al., 2013, MNRAS, 435, 329

Lundqvist P. et al., 2015, A&A, 577, A39

Maguire K. et al., 2013, MNRAS, 436, 222

Maguire K., Taubenberger S., Sullivan M., Mazzali P. A., 2016, MNRAS, 457, 3254

Maguire K. et al., 2018, MNRAS, 477, 3567

Maoz D., Mannucci F., Nelemans G., 2014, ARA&A, 52, 107

Marion G. H. et al., 2016, ApJ, 820, 92

Mattila S., Lundqvist P., Sollerman J., Kozma C., Baron E., Fransson C., Leibundgut B., Nomoto K., 2005, A&A, 443, 649

Mazzali P. A. et al., 2015, MNRAS, 450, 2631

Müller-Bravo T. E. et al., 2022, A&A, 665, A123

Pan K.-C., Ricker P. M., Taam R. E., 2012, ApJ, 760, 21

Papadogiannakis S., Dhawan S., Morosin R., Goobar A., 2019, MNRAS, 485, 2343

Pastorello A. et al., 2007, MNRAS, 377, 1531

Perlmutter S., Turner M. S., White M., 1999, Phys. Rev. Lett., 83, 670

Phillips M. M., Phillips, M. M., 1993, ApJL, 413, L105

Prieto J. L. et al., 2020, ApJ, 889, 100

Pskovskii I. P., 1977, Soviet Astronomy, 21, 675

Riess A. G. et al., 1998, AJ, 116, 1009

Riess A. G. et al., 2016, ApJ, 826, 56

Ruiter A. J., 2020, IAUS, 357, 1

Rust B. W., 1974, PhD thesis

Sabbi E. et al., 2018, ApJS, 235, 23

Sai H. et al., 2022, MNRAS, 514, 3541

Sand D. J. et al., 2016, ApJ, 822, L16

Schlafly E. F., Finkbeiner D. P., 2011, ApJ, 737, 103

Shappee B. J., Stanek K. Z., 2011, ApJ, 733, 124

Shappee B. J., Stanek K. Z., Pogge R. W., Garnavich P. M., 2013, ApJL, 762, L5

Shappee B. J., Stanek K. Z., Kochanek C. S., Garnavich P. M., 2017, ApJ, 841, 48h

Shen K. J., Kasen D., Miles B. J., Townsley D. M., 2018, ApJ, 854, 52

Shingles L. J., Flörs A., Sim S. A., Collins C. E., Roepke F. K., Seitenzahl I. R., Shen K. J., 2022, MNRAS, 512, 6150

Silverman J. M. et al., 2013, ApJS, 207, 3

Smartt S. J. et al., 2015, A&A, 579, A40

Sollerman J. et al., 2004, A&A, 428, 555

Sorce J. G., Tully R. B., Courtois H. M., Jarrett T. H., Neill J. D., Shaya E. J., 2014, MNRAS, 444, 527

Stritzinger M., Sollerman J., 2007, A&A, 470, L1

Taubenberger S., 2017, in Alsabti A. W., Murdin P., eds, Handbook of Supernovae. Springer International Publishing AG, Cham, p. 317

Theureau G., Hanski M. O., Coudreau N., Hallet N., Martin J.-M., 2007, A&A, 465, 71

Tonry J. L., Dressler A., Blakeslee J. P., Ajhar E. A., Fletcher A. B., Luppino G. A., Metzger M. R., Moore C. B., 2001, ApJ, 546, 681

Tucker M. A., Shappee B. J., Kochanek C. S., Stanek K. Z., Ashall C., Anand G. S., Garnavich P., 2022, MNRAS, 517, 4119

Tully R. B., 1988, Nearby Galaxies Catalog. Cambridge Univ. Press, Cambridge

Tully R. B., Rizzi L., Shaya E. J., Courtois H. M., Makarov D. I., Jacobs B. A., 2009, AJ, 138, 323

Tully R. B. et al., 2013, AJ, 146, 86

Turatto M., Benetti S., Cappellaro E., Danziger I. J., Della Valle M., Gouiffes C., Mazzali P. A., Patat F., 1996, MNRAS, 283, 1

Vernet J. et al., 2011, A&A, 536, A105

Vinko J. et al., 2012, A&A, 546, A12

Vinkó J. et al., 2018, PASP, 130, 064101

Walker E. S. et al., 2015, ApJS, 219, 13

Wang X., Wang L., Filippenko A. V., Zhang T., Zhao X., 2013, Science, 340, 170

Wilk K. D., Hillier D. J., Dessart L., 2018, MNRAS, 474, 3187

Wood-Vasey W. M. et al., 2008, ApJ, 689, 377

Yamanaka M. et al., 2014, ApJ, 782, L35

Yang Y. et al., 2020, ApJ, 902, 46

Zhai Q. et al., 2016, AJ, 151, 125

Zhang J.-J., Wang X.-F., Bai J.-M., Zhang T.-M., Wang B., Liu Z.-W., Zhao X.-L., Chen J.-C., 2014, AJ, 148, 1

SUPPORTING INFORMATION

Supplementary data are available at *MNRAS* online.

HST_photometry_table_updated.csv
Photometry_table_updated.csv

Please note: Oxford University Press is not responsible for the content or functionality of any supporting materials supplied by the authors. Any queries (other than missing material) should be directed to the corresponding author for the article.

APPENDIX A: SAMPLE OVERVIEW

Table A1. A table summarizing the SNe Ia present in our sample, showing the classification of the SN, redshift, distance modulus, and time of maximum light. We also include optical and cosmological parameters (M_{max}^B, x_1, and c) and the source of the NIR photometry/spectroscopy.

SN	z	μ [mag]	t_{max}^B [d]	$E(B-V)_{gal}$ [mag]	M_{max}^B [mag]	x_1	c	Data Ref.[a]	Dist. ref.[b]
SN2000cx[c]	0.00818	32.87 ± 0.21	51752.1	0.082	−19.77 ± 0.21	0.08 ± 0.12	0.043 ± 0.003	[1], [2]	[24]
SN2001el	0.003896	31.65 ± 0.35	52181.9	0.014	−18.88 ± 0.35	0.04 ± 0.02	0.191 ± 0.002	[3], [4]	[25]
SN2003hv	0.005624	31.37 ± 0.30	52891.7	0.016	−18.99 ± 0.35	−1.95 ± 0.01	−0.110 ± 0.002	[5]	[26], [27]
SN2004eo[d]	0.016	34.12 ± 0.10	53278.1	0.108	−19.06 ± 0.10	−1.18 ± 0.01	0.169 ± 0.001	[6]	[28]
SN2011fe	0.0006	29.04 ± 0.05	55814.6	0.009	−19.09 ± 0.06	−0.51 ± 0.02	−0.022 ± 0.003	[7], [8]	[29]
SN2012cg*	0.0015	30.83 ± 0.05	56082.2	0.200	−19.55 ± 0.05	0.77 ± 0.05	0.071 ± 0.005	[9], [10]	[30]
SN2012fr	0.005	31.38 ± 0.06	56241.9	0.020	−19.45 ± 0.07	1.66 ± 0.01	−0.084 ± 0.001	[11], [13]	[31]
SN2012ht[e]	0.003	31.91 ± 0.04	56295.1	0.029	−18.30 ± 0.40	−1.37 ± 0.03	0.120 ± 0.005	[11], [12], [14]	[32]
SN2013aa	0.003	30.72 ± 0.05	56342.5	0.170	−19.73 ± 0.05	0.36 ± 0.01	0.026 ± 0.001	[9], [15]	[33]
SN2013cs	0.009	32.94 ± 0.14	56437.2	0.093	−19.33 ± 0.14	0.29 ± 0.02	0.116 ± 0.002	[9]	[34]
SN2013ct	0.003	30.27 ± 0.20	56416.1	0.028	− ± −	− ± −	− ± −	[9]	[34]
SN2013dy	0.003889	31.54 ± 0.08	56501.7	0.350	−19.70 ± 0.08	0.92 ± 0.02	0.283 ± 0.002	[9], [12], [16]	[32]
SN2014J	0.000677	27.74 ± 0.08	56689.0	0.050	−19.19 ± 0.10	0.87 ± 0.01	1.198 ± 0.001	[12], [17]	[35]
SN2016hvl	0.0131	33.76 ± 0.40	57710.9	0.438	−18.40 ± 0.40	0.23 ± 0.01	0.458 ± 0.001	[18]	[36]
SN2017cbv*	0.003	31.14 ± 0.40	57841.3	0.169	−20.13 ± 0.40	0.62 ± 0.01	0.082 ± 0.001	[18], [19]	[37]
SN2017erp	0.006174	32.34 ± 0.10	57934.6	0.100	−19.12 ± 0.10	0.18 ± 0.01	0.175 ± 0.001	[9], [12], [20], [21]	[38]
SN2018gv	0.005274	31.71 ± 0.40	58149.6	0.058	−19.14 ± 0.40	0.717 ± 0.002	−0.0059 ± 0.0002	[12], [22]	[36]
SN2019np*	0.00452	32.87 ± 0.43	58507.6	0.020	−19.57 ± 0.43	−0.86 ± 0.03	−0.013 ± 0.002	[12], [23]	[39]
SN2020ees	0.024424	35.16 ± 0.40	58926.1	0.014	−19.10 ± 0.45	0.39 ± 0.48	0.024 ± 0.060	[18]	[36]
SN2020uxz**	0.00825	32.10 ± 0.43	59143.0	0.038	−18.68 ± 0.43	0.66 ± 0.03	0.005 ± 0.004	[18]	[39]
SN2021jad	0.005534	31.87 ± 0.43	59328.7	0.035	−19.16 ± 0.43	0.30 ± 0.03	0.028 ± 0.003	[18]	[39]
SN2021pit	0.004	31.31 ± 0.05	59384.5	0.014	−19.04 ± 0.05	−0.34 ± 0.02	0.027 ± 0.002	[18]	[32]
SN2021wuf	0.01	33.61 ± 0.40	59461.1	0.090	−20.01 ± 0.40	−0.08 ± 0.02	−0.136 ± 0.002	[18]	[36]
SN2021aefx*	0.005017	31.27 ± 0.49	59545.9	0.009	−19.19 ± 0.49	0.82 ± 0.01	0.002 ± 0.001	[18]	[40]

Notes. [a] Sources of photometry and spectroscopy: (1) Sollerman et al. (2004), (2) Li et al. (2001), (3) Stritzinger & Sollerman (2007), (4) Krisciunas et al. (2003), (5) Leloudas et al. (2009), (6) Pastorello et al. (2007), (7) Shappee et al. (2017), (8) Vinkó et al. (2012), (9) Maguire et al. (2016), (10) Marion et al. (2016), (11) Maguire et al. (2013), (12) Graur et al. (2020), (13) Zhang et al. (2014), (14) Vinkó et al. (2018), (15) Burns et al. (2020), (16) Zhai et al. (2016), (17) Sand et al. (2016), (18) this paper, (19) Hosseinzadeh et al. (2017), (20) Clark et al. (2021), (21) Brown et al. (2019), (22) Yang et al. (2020), (23) Sai et al. (2022). [b] Sources for redshift-indepedent distance moduli: (24) Li et al. (2001), (25) Krisciunas et al. (2003), (26) Tonry et al. (2001), (27) Jensen et al. (2003), (28) Shappee & Stanek (2011), (29) Pastorello et al. (2007), (30) Vinkó et al. (2018), (31) Tully et al. (2009), (32) Riess et al. (2016), (33) Jacobson-Galán et al. (2018), (34) Walker et al. (2015), (35) Tully et al. (2013), (36) Theureau et al. (2007), (37) Könyves-Tóth et al. (2020), (38) Tully (1988), (39) Sorce et al. (2014), (40) Sabbi et al. (2018). [c] SN 2000cx is spectroscopically classified as a 91T-like SN Ia, but it shows unusual asymmetry in its *B*-band light curve and its spectral evolution is unlike that of the rest of the subclass (Li et al. 2001). These peculiarities have been attributed to a larger ^{56}Ni mass and higher kinetic energy in the explosion (Li et al. 2001). [d] SN 2004eo is likely a transitional SN Ia, with properties similar to SN 2004eo (Yamanaka et al. 2014). [e] SN 20012ht is also a transitional SN Ia (Pastorello et al. 2007).

* A flux excess has been detected in the early light curve.

** We tentatively find a flux excess in the SWIFT data for this light curve, see discussion in Section 5.3.

APPENDIX B: USE OF DERIVATIVES TO ANALYSE THE EVOLUTION DURING THE PLATEAU

It is clear from Fig. 2 that there is an evolution in the decline rate for model 1, and finding the average decline rate across the plateau ignores such evolution. To analyse this evolution, we fit the models with a univariate spline and calculate the first- and second-order derivatives with respect to the phase, presented in Fig. B1. Although the *J* and *H* bands both approach a slope of zero around 300 d, the slope in *H* is steeper prior to this and there is a larger change in the first derivative between 150 and 300 d than in the *J* band. After the minimum is reached, the shape of the first derivative is similar between the two bands.

The only SNe Ia with sufficient data to capture the full evolution across the plateau are SNe 2017erp and 2018gv. SN 2014J has data spanning 350–500 d, but we exclude it here because the photometry is synthetic and shows unusual evolution, although it is consistent with the evolution of SNe 2017erp and 2018gv within its uncertainties. We include the light curves of SNe 2017erp and 2018gv, the spline fits, and derivatives in Fig. B1. The first derivative of the light curve of SN 2017erp matches exceptionally well with the model, whilst SN 2018gv reaches its minimum in the first derivative slightly later. Similarly, the inflection points in the light curves, located where the second derivative equals zero, occur at the same time for the model and SN 2017erp, whereas SN 2018gv reaches the inflection point 10 d later. We note that when measuring the decline rate for the remainder of the sample (see Fig. 3), those with data at a later stage (200 + d) have a shallower decline as discussed in Section 4.1.2.
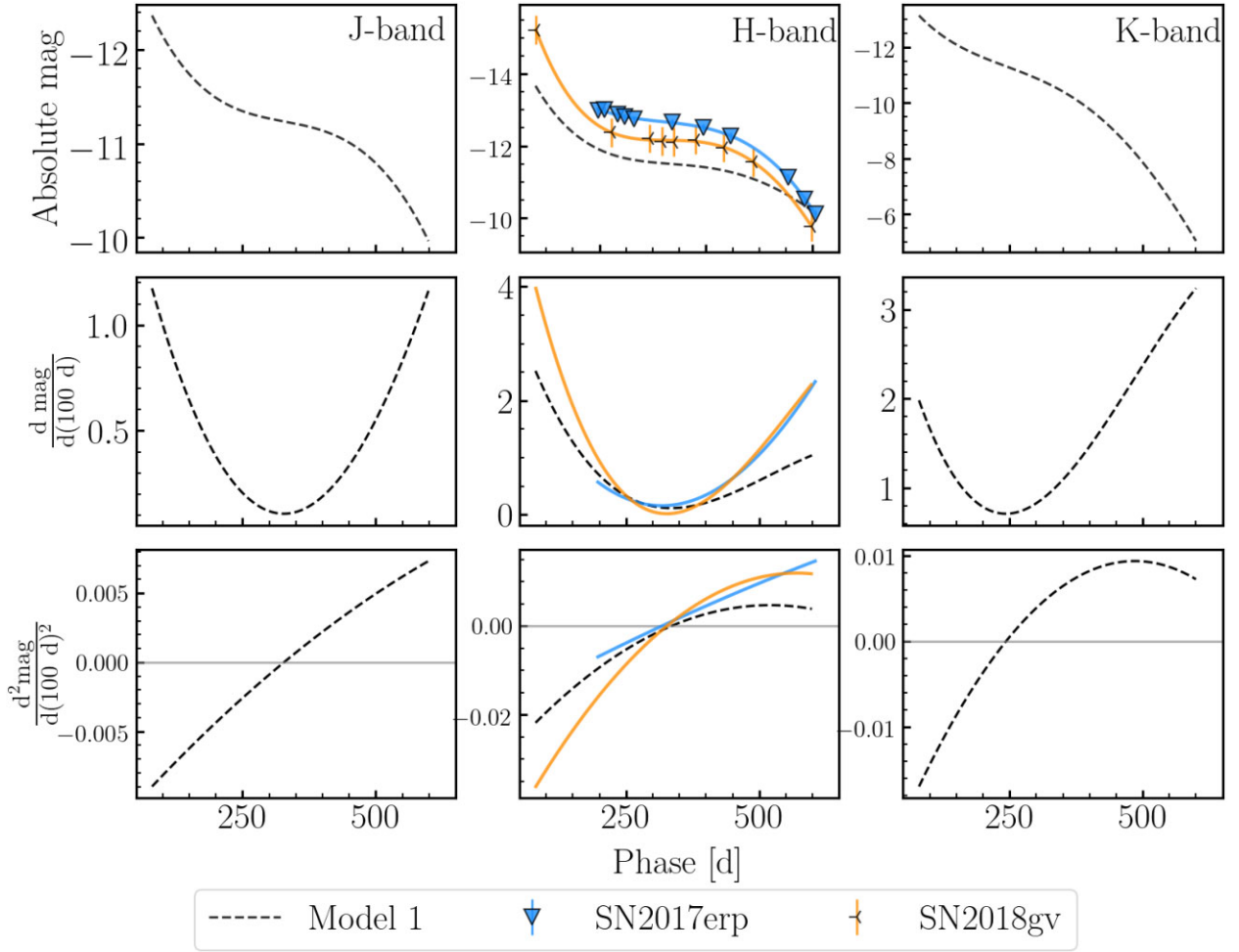

Figure B1. *Top panels:* The light curves in *J*, *H*, and K_s bands of model 1, as well as SNe 2017erp and 2018gv. All light curves are fit using a univariate spline, and the resulting fits are plotted as a dashed line for the model and solid lines for the SNe Ia. *Middle panels:* The first derivative of the apparent magnitude with respect to time. *Bottom panels:* The second derivative of the apparent magnitude with respect to time. We denote where the second derivative equals zero with a grey line, since where this line meets the second derivative indicates the inflection point in the light curve. Model 1 and SN 2017erp both reach an inflection point at 317 d, whilst SN 2018gv reaches an inflection point at 327 d.

[1] *School of Physics, Trinity College Dublin, College Green, Dublin 2, Ireland*

[2] *Institute of Cosmology and Gravitation, University of Portsmouth, Portsmouth, PO1 3FX, UK*

[3] *Department of Astrophysics, American Museum of Natural History, Central Park West and 79th Street, New York, NY 10024, USA*

[4] *GSI Helmholtzzentrum für Schwerionenforschung, Planckstraße 1, D-64291 Darmstadt, Germany*

[5] *School of Physics, University College Dublin, Belfield, Dublin 4, Ireland*

[6] *Department of Astronomy, The Oskar Klein Center, Stockholm University, AlbaNova, SE-106 91 Stockholm, Sweden*

[7] *European Southern Observatory, Alonso de Córdova 3107, Casilla 19, Santiago, Chile*

[8] *Millennium Institute of Astrophysics MAS, Nuncio Monsenor Sotero Sanz 100, Off. 104, Providencia, Santiago, Chile*

[9] *Las Cumbres Observatory, 6740 Cortona Dr Suite 102, Goleta, CA, 93117, USA*

[10] *Department of Physics, University of California, Santa Barbara, CA 93106-9530, USA*

[11] *Technische Universität München, TUM School of Natural Sciences, Physik-Department, James-Franck-Straße 1, D-85748 Garching, Germany*

[12] *Max-Planck-Institut für Astrophysik, Karl-Schwarzschild Straße 1, D-85748 Garching, Germany*

[13] *Institute of Space Sciences (ICE, CSIC), Campus UAB, Carrer de Can Magrans, s/n, E-08193 Barcelona, Spain*

[14] *Institut d'Estudis Espacials de Catalunya (IEEC), E-08034 Barcelona, Spain*

[15] *School of Physics and Astronomy, University of Southampton, Southampton, SO17 1BJ, UK*

[16] *Institute of Astronomy and Kavli Institute for Cosmology, Madingley Road, Cambridge, CB3 0HA, UK*

[17] *Finnish Centre for Astronomy with ESO (FINCA), FI-20014 University of Turku, Finland*

[18] *Tuorla Observatory, Department of Physics and Astronomy, FI-20014 University of Turku, Finland*

[19] *Center for Astrophysics, Harvard & Smithsonian, 60 Garden Street, Cambridge, MA 02138-1516, USA*

[20] *The NSF AI Institute for Artificial Intelligence and Fundamental Interactions, USA*

[21] *Cardiff Hub for Astrophysics Research and Technology, School of Physics & Astronomy, Cardiff University, Queens Buildings, The Parade, Cardiff, CF24 3AA, UK*

[22] *Department of Physics, University of Warwick, Gibbet Hill Road, Coventry CV4 7AL, UK*

[23] *Birmingham Institute for Gravitational Wave Astronomy and School of Physics and Astronomy, University of Birmingham, Birmingham B15 2TT, UK*

[24] *Isaac Newton Group (ING), Apt. de correos 321, E-38700, Santa Cruz de La Palma, Canary Islands, Spain*

[25] *Astrophysics Research Centre, School of Mathematics and Physics, Queen's University Belfast, Belfast BT7 1NN, UK*

This paper has been typeset from a TEX/LATEX file prepared by the author.